

PHOTOEVAPORATION OF COSMOLOGICAL MINIHALOS  
BY THE FIRST STARS

by

Joseph Smidt

A senior thesis submitted to the faculty of  
Brigham Young University  
in partial fulfillment of the requirements for the degree of

Bachelor of Science

Department of Physics and Astronomy

Brigham Young University

August 2007

Copyright © 2007 Joseph Smidt

All Rights Reserved

BRIGHAM YOUNG UNIVERSITY

DEPARTMENT APPROVAL

of a senior thesis submitted by

Joseph Smidt

This thesis has been reviewed by the research advisor, research coordinator,  
and department chair and has been found to be satisfactory.

\_\_\_\_\_  
Date

\_\_\_\_\_  
David Neilsen, Advisor

\_\_\_\_\_  
Date

\_\_\_\_\_  
Eric Hintz, Research Coordinator

\_\_\_\_\_  
Date

\_\_\_\_\_  
Ross L. Spencer, Chair

ABSTRACT

PHOTOEVAPORATION OF COSMOLOGICAL MINIHALOS  
BY THE FIRST STARS

Joseph Smidt

Department of Physics and Astronomy

Bachelor of Science

We perform two-dimensional simulations of cosmological minihalo evaporation in the vicinity of a Population III star to determine if its ultraviolet (UV) radiation promotes or quenches star formation in nearby primordial clouds. We find that the ionization front of the star penetrates nearby halos to varying degrees according to their central density and proximity to the star. UV photons easily destroy diffuse clouds but cannot affect the cores of denser, more evolved structures. In intermediate cases, the radiation drives shocks enriched with  $\text{H}_2$ , a key coolant in primeval gas, into the core. These shocks enhance density and cooling rates in the halo core, accelerating its collapse into a new star. Radiative feedback by one primordial star on subsequent star formation can thus be positive, negative, or neutral.

## ACKNOWLEDGMENTS

I would like to thank Dr. Daniel Whalen of the Theoretical Astrophysics Group T-6 at Los Alamos National Laboratory for guiding my research both at the lab and when I returned home to BYU. He was very helpful with mentoring multiple projects and assisting in the writing process. This work could not have been completed without his help.

I would like to also thank Dr. David Neilsen of Brigham Young University for mentoring research I have done at BYU as well as assisting in the writing process. Many of my research accomplishments, including this work, would not have been done without his assistance.

I would like to thank my wife Esther, parents, grandparents and all other family, especially Mike and Sandra Smidt, Dave and Sheri Turley, Ron and Sharon Cole, Joe and Barbra Smidt, Richard and Jean Turley, Garn and Geniel Christensen, and my great-grandpa Bill Cole and his wife Sally for their much needed support while I have been a student here at BYU.



# Chapter 1

## Introduction

Observational studies indicate that the universe is composed of 74% dark energy, 22% dark matter, and 4% baryonic matter [1–5]. After the Big Bang and a brief period of rapid inflationary growth the universe was hot, ionized, and largely featureless [1,6–9]. As the universe expanded it cooled, reaching temperatures at which ions and nuclei could combine into neutral atoms at a redshift<sup>1</sup>  $z$  of  $\sim 1300$ , or  $\sim 400,000$  yr after the Big Bang. Gaussian fluctuations in quantum fields dimpled the otherwise uniform dark matter; as the universe continued to expand, gravity collapsed these perturbations into a vast network of filaments, sheets and halos<sup>2</sup> on megaparsec<sup>3</sup> scales (see Fig. 1.1) [1,6–11]. Dark matter halos grew with time as they collided and merged with other halos. This process led to the cosmic web of galaxies and clusters of galaxies observed today in deep field surveys like the Two Degree Field Galaxy Redshift Survey (2dF) and the Sloan Digital Sky Survey (SDSS) [12–14]. Dark matter dominated the gravitational dynamics of the universe rather than primordial

---

<sup>1</sup>Redshift, denoted by the variable  $z$ , is a numerical value signifying how much light from an object is redshifted and hence how far away it is.

<sup>2</sup>A halo is a roughly spherical clump of dark matter

<sup>3</sup>1 parsec = 3.26 light-years

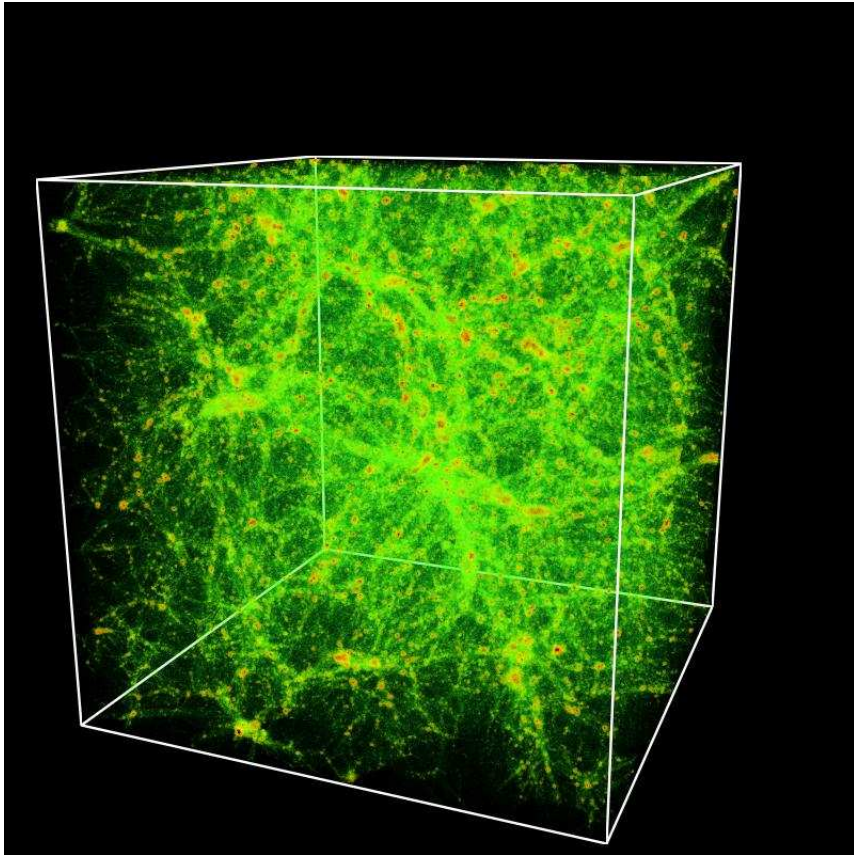


**Figure 1.1** The cosmic network of dark matter filaments and halos in a  $100/h$  Mpc simulation box with  $512^3$  zones, courtesy of Renyue Chen ([www.astro.princeton.edu/~cen/PROJECTS/p1/p1.html](http://www.astro.princeton.edu/~cen/PROJECTS/p1/p1.html))

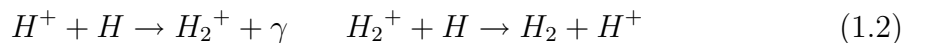
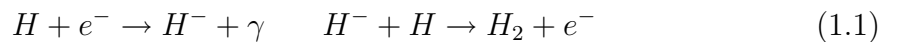
gas because of its greater abundance, but primordial gas traced the distribution of dark matter because it was gravitationally drawn to it. Dark matter halos thus harbored clouds of primordial H and He.

## 1.1 Formation of the First Stars

When cosmological minihalos grew to  $\sim 10^6$  solar masses (dark matter + gas), primordial gas clouds within them could condense and form the first stars at  $z \sim 20\text{--}30$ , or approximately 200 million years after the Big Bang. Numerical simulations indi-

cate that these stars (which predated the formation of primitive galaxies by several hundred million years) were likely very massive, 100 to 500 solar masses ( $M_{\odot}$ ), and that they formed one per halo [15, 16]. They had correspondingly short lifetimes of 2–3 Myr and were millions of times more luminous than the Sun due to surface temperatures in excess of 100,000 K. These Population III (or Pop III) stars were also intense sources of ionizing ultraviolet (UV) photons with energies above 13.6 eV.

As a primordial gas cloud contracted to form a star, infalling gas atoms collided more frequently in the core. The ordered motion of infall became disordered atomic motion, manifest as heat, or pressure. As central pressures rose, further infall was curtailed, and the cloud could not shrink any further unless some mechanism removed heat from its center. In star-forming clouds in the galaxy today, gas atoms collide with dust grains, which radiate infra-red (IR) photons that transport heat out of the cloud and allow it to contract. No dust was present in the pristine H and He of primordial minihalos; instead, chemical reactions manufactured molecular hydrogen ( $H_2$ ) through two gas phase reactions:



$H_2$  molecules exhibit rotational and vibrational modes that can be stimulated by collisions with H and He and later de-excite through the emission of IR photons. These photons exit the cloud and allow the cloud to collapse into a star. Primordial stars were much more massive than their 1–100  $M_{\odot}$  descendants in the galaxy today because the much lower efficiency of  $H_2$  cooling led to far higher accretion rates onto the central protostar.

## 1.2 Impact of Pop III Stars on Their Environment

The dark matter minihalos hosting the first stars tended to group in small swarms, an effect known as cluster bias. An important, unanswered question in cosmology is the effect one massive star in a halo had on subsequent star formation in nearby halos. Hard UV photons from a Pop III star cannot simply stream into space unimpeded because they are capable of ionizing H and He gas. Instead, they propagate into the intergalactic medium (IGM) behind an abrupt wall of radiation known as an ionization front (or I-front). The gas behind the front is nearly completely ionized and, because of the structure of the H and He cooling curves, is at 20,000 to 30,000 K. I-fronts can drive strong hydrodynamical shocks that can sweep over neighbor halos and disrupt them.

Also, just as their high temperatures made them extremely luminous sources of ionizing UV, these stars also emitted large numbers of UV photons in the Lyman-Werner (LW) band (11.18–13.6eV). These photons dissociate 15% of the H<sub>2</sub> molecules they encounter and can travel great distances in the IGM because H gas is transparent to them. LW radiation outruns the I-front of the massive star and can sterilize nearby halos of the H<sub>2</sub> required for cloud collapse. Both of these effects can pre-empt star formation in halos in the vicinity of the Pop III star and are known as *negative* radiative feedback. Also, the high temperatures of the ionized gas (known as an H II region) in general can postpone new star formation [17].

However, after the central star dies the H II region begins to recombine into neutral gas atoms, emitting photons below the ionization energy of H and thereby cooling. This cooling proceeds out of equilibrium in the sense that the gas cools faster than it recombines [18]. The result is a vast field of primordial gas that has cooled to a few thousand K with ionized fractions on the order of 10% that persist for tens of

millions of years. Such conditions are fertile for molecular hydrogen production by the H- channel described in Eq. 1 above. Rapid H<sub>2</sub> production ensues, cooling the relic H II region and allowing new gas clouds to form that are gravitationally unstable to collapse, possibly into a new generation of stars. This postmortem promotion of star formation by the original Pop III star is known as *positive* radiative feedback.

Another radiative feedback channel surprisingly may be the I-front that sweeps over the proximate halo. The front itself is not a perfect discontinuity between the ionized postfront gas and the upstream neutral gas: high energy photons penetrate slightly ahead and pre-ionize the gas, creating again ideal conditions for the formation of molecular hydrogen [19]. As the front approaches the neighbor halo, the H<sub>2</sub> layer can shield the halo from LW photons from the massive star, allowing H<sub>2</sub> to once again form in and cool the core of the halo. After the death of the star, the remnant shock, highly enriched with H<sub>2</sub>, may merge with the core of the halo, adding additional coolant to it and hastening its collapse into a star.

### 1.3 Numerical Simulation of Radiative Feedback

At present, it is unknown if these feedback processes promote or quench star formation in minihalos proximate to Pop III stars. First structure formation began at redshifts (and thus times) beyond the access of current telescope technology, so one must resort to numerical simulations on supercomputers to determine their final outcomes. Calculations of radiative feedback in large scale structure formation (on the scales of galaxies and galactic clusters) indicate that the rise of an intergalactic Lyman-Werner background from the first generation of Pop III stars at most postponed later generations of stars [20, 21]. Other simulations suggest positive feedback dominates on large scales, but these studies were limited by inadequate spatial resolution [22, 23].

More recently, feedback from a single star upon neighboring halos in its cluster has been examined. Susa and Umemura [24, 25] studied the photoevaporation of an idealized halo by a nearby Pop III star to assess the survival of  $\text{H}_2$  in the halo [24]. They found that  $\text{H}_2$  may or may not remain in the satellite halo, depending on a variety of factors, including its distance to the parent star and the central density of the illuminated halo. O’Shea, *et al* considered the evolution of a satellite halo assumed to be ionized by a Pop III star [26]. They discovered a second star forms in the recombining halo, but this result did not include the hydrodynamic history of the photoevaporated cloud. Ahn and Shapiro performed a 1D radiation hydrodynamical simulation of halos photoionized by a primordial star [25] and found that photoevaporation under certain circumstances promoted  $\text{H}_2$  formation in the halo core and its subsequent collapse after the death of the ionizing source. However, an improper coordinate mesh introduced serious errors in the evolution of their halo core that will likely invalidate many of their central conclusions.

## 1.4 Overview

We present 2D numerical simulations of the photoevaporation of cosmological mini-halos clustered around a single primordial star. Our calculations incorporate self-consistent transport of ionizing UV and LW photons together with 9-species primordial gas chemistry and cooling. We follow the hydrodynamical evolution of the halos and their  $\text{H}_2$  fractions over the main sequence lifetime of the central star as well as in the relic H II region that persists thereafter. In Chapter Two we describe the ZEUS-MP code, the physics in our calculations, and the initial conditions for the simulations. We discuss our results and conclude in Chapter Three.

# Chapter 2

## Numerical Algorithm and Problem Setup

### 2.1 ZEUS-MP Astrophysical Fluid Hydrodynamics Code

Our numerical algorithm is a modified version of the ZEUS-MP astrophysical fluid hydrodynamics code. Developed at the University of Illinois at Urbana-Champaign (UIUC) and University of California, San Diego (UCSD), ZEUS-MP [27] finite-differences Euler's equations of fluid dynamics:

$$\frac{\partial \rho}{\partial t} = -\nabla \cdot (\rho \mathbf{v}), \quad (2.1)$$

$$\frac{\partial \rho v_i}{\partial t} = -\nabla \cdot (\rho v_i \mathbf{v}) - \nabla p - \rho \nabla \Phi - \nabla \cdot \mathbf{Q}, \quad (2.2)$$

$$\frac{\partial e}{\partial t} = -\nabla \cdot (e \mathbf{v}) - p \nabla \cdot \mathbf{v} - \mathbf{Q} : \nabla \mathbf{v}, \quad (2.3)$$

where  $\rho$ ,  $e$ , and  $v_i$  are the mass density, internal energy density, and velocity components, respectively, and  $p = (\gamma - 1)e$  and  $\mathbf{Q}$  are the gas pressure and von Neumann-Richtmeyer artificial viscosity. These equations describe mass, momentum, and energy conservation in the fluid, respectively. ZEUS-MP evolves the left hand side of each equation, term by term, using a method known as operator splitting. The gradient (force) terms represent changes at a point due to forces acting upon a zone and are calculated in the source routines. The divergence terms, which represent changes in fluid quantities from material being carried into or away from the zone due to flow, are calculated by advection routines. ZEUS-MP can solve these equations in one, two, or three dimensions on cartesian, cylindrical, or spherical coordinate meshes.

## 2.2 Primordial Chemistry/Radiative Transfer

The ZEUS-MP employed in our simulations incorporates a 9-species reaction network (for H, H<sup>+</sup>, He, He<sup>+</sup>, He<sup>2+</sup>, H<sup>-</sup>, H<sub>2</sub><sup>+</sup>, H<sub>2</sub>, and e<sup>-</sup>) and photon-conserving UV radiative transfer not available in the public release. Over 70 chemical reactions can occur in primordial H and He gas; we follow the 30 most important with nine additional mass conservation equations and the nonequilibrium rate equations of Anninos *et al.* [28, 29]:

$$\frac{\partial \rho_i}{\partial t} = -\nabla \cdot (\rho \mathbf{v}) + \sum_j \sum_k \beta_{jk}(T) \rho_j \rho_k + \sum_j \kappa_j \rho_j. \quad (2.4)$$

$\beta_{jk}$  is the rate coefficient between species  $j$  and  $k$  which creates (+) or removes (-) species  $i$ . The divergence terms are calculated in the advection routines while the network is evolved in a separate routine.

The current version of ZEUS-MP can transport UV photons from a point source at the center of a spherical coordinate (RTP) mesh or evolve plane waves along the x-axis of a cartesian (XYZ) box or along the z-axis of a cylindrical coordinate (ZRP)

system. In RTP coordinates radial rays are cast from the point source at the origin to the outer boundary of the grid; each cell is pierced along the way. Plane waves are transported by casting rays parallel to the x- or z-axis. A given ray begins in a cell on the lower boundary and extends to the opposite cell on the upper boundary. The equation of radiative transfer is then solved along each ray to obtain the radiative rate coefficients in each cell that appear in the reaction network above. The equation of transfer [30]:

$$\frac{1}{c} \frac{\partial I_\nu}{\partial t} + \hat{\mathbf{n}} \cdot \nabla I_\nu = \eta_\nu - \chi_\nu I_\nu \quad (2.5)$$

can be simplified through a series of well-motivated steps to obtain the static approximation:

$$\hat{\mathbf{n}} \cdot \nabla I_\nu = -\chi_\nu I_\nu \quad (2.6)$$

where  $I(t, \mathbf{x}, \hat{\mathbf{n}}, \nu)$  is the specific intensity of the radiation field at the position  $\mathbf{x}$  approaching from the direction  $\hat{\mathbf{n}}$ . The parameters  $\eta_\nu$ ,  $\chi_\nu$ , and  $c$  represent the emission coefficient, the absorption coefficient and the speed of light respectively. The static approximation permits us to dispense with the time derivative, which would restrict solutions to the equation to far shorter time steps than are required for accuracy in most cosmological applications.

## 2.3 Energy Equation

We account for the photoionizational heating and six cooling processes that accompany our chemistry and radiation models with an added gas energy equation:

$$\dot{e}_{gas} = \Gamma - \Lambda \quad (2.7)$$

$\Gamma$  is the photoheating rate and  $\Lambda$  is the sum of six cooling processes: electron collisional and ionizational cooling, recombinational cooling,  $\text{H}_2$  cooling, bremsstrahlung cooling,

and Compton cooling. Electrons can collide with neutral atoms, either exciting them (with subsequent photon emission) or completely removing an electron from them. In either case, there is a net loss of kinetic energy from the original electron, which cools the gas. When an ion recombines, it removes an energetic electron from the gas, thereby reducing its temperature. Bremsstrahlung occurs when energetic free electrons in a gas are deflected by the positive nuclei of ions, emitting a photon in the process at the expense of their own kinetic energy.  $\text{H}_2$  cooling was described earlier, and Compton cooling occurs when free electrons collide with cosmic microwave background (CMB) photons at high redshifts, imparting energy to them while slowing down themselves. All six processes can operate in primordial gas.

## 2.4 Time Step Control

The differential equations governing the fluid equations, chemistry, and radiative transfer exhibit distinct characteristic time scales that can be highly disparate. To evolve each set of equations according to its own time scale while avoiding restricting the entire set to unnecessarily short time steps, we adopt a hierarchical update scheme. The equation of transfer, reaction network, and gas energy equation are evolved over a photoionization time scale:

$$t_{chem} = \frac{n_e}{\dot{n}_e} \quad (2.8)$$

These updates are repeated until a photoheating/cooling time scale has been crossed:

$$t_{heat} = \frac{e_{gas}}{\dot{e}_{heat/cool}} \quad (2.9)$$

at which point the equations of hydrodynamics are solved to yield new gas densities, energies, and velocities. The global minimum time scale of the entire grid is chosen at each stage to ensure that the solution to the system in one region of the grid does not outpace the solution in other regions; thus, global solution concurrency is enforced.

## 2.5 Problem Setup/Initial Conditions

We perform five runs simulating a Pop III star photoevaporating a neighboring halo. The runs differ in halo type. The first is a semi-analytical  $2.0 \times 10^5 M_{\odot}$  truncated isothermic sphere (TIS) halo. It is spherically symmetric and is 540 pc from a  $120 M_{\odot}$  Pop III star. The other four halos are formed from cosmological initial conditions in the publicly available adaptive mesh refinement (AMR) code Enzo. Enzo follows the collapse of ripples in primordial dark matter from a redshift of  $z=99$  down to the redshift at which the halo can first form a star ( $\sim 20$ ) using the equations of dark matter dynamics, gas dynamics, and 9-species non-equilibrium primordial chemistry. We evaporate these halos at several distances from a  $120 M_{\odot}$  Pop III star specified below. We choose a  $120 M_{\odot}$  star since it is representative of 100–500 Pop III stars but will not explode as a Type II or pair-instability supernova [31].

After being formed in Enzo, each halo is centered in a 2D cylindrical  $zr$  box in ZEUS-MP. The inner and outer mesh boundaries are -125 pc and 125 pc in  $z$  and 0.01 pc and 125 pc in  $r$ . The grid has 1000 zones in the  $z$ -direction and 500 in the  $r$ -direction, yielding a grid resolution of 0.25 pc. Dark matter is not present in the simulations but its gravity is included by setting the gas halo in hydrostatic equilibrium (balancing pressure forces with gravity so the halo sits still).

A plane wave of photons from a nearby Pop III star enters the lower  $z$  face of the box and sweeps across the halo. We attenuate the plane wave intensity with a  $\frac{1}{R^2}$  falloff where  $R$  is the distance from the illuminating star. The luminosity of the star is  $10^{6.243} L_{\text{solar}}$  and has a surface temperature of  $9.572 \times 10^4$  K. The energy distribution of the photons is blackbody and is partitioned into two groups. The first group contains 40 frequency bins equally spaced in energy between 0.755 eV and 13.6 eV. These photons cannot ionize hydrogen but do drive a variety of photochemical

reactions including the dissociation of  $\text{H}_2$ . The second group contains 80 frequency bins logarithmically spaced between 13.6 eV and 90 eV. This multifrequency spectrum captures the true structure of the I-front, especially the hard photon broadening of the front in which  $\text{H}_2$  layers can form.

The halo is initialized with a free electron fraction of  $10^{-4}$  and an  $\text{H}_2$  fraction of  $2 \times 10^{-6}$   $\text{H}_2$ , consistent with the IGM at a redshift of  $z = 20$ . The gas in the halo is 76% hydrogen and 24% helium by mass, in accordance with Big Bang nucleosynthesis (BBN). ZEUS-MP ensures that the cooling curves do not drop the gas temperature below 57.3 K, the temperature of the cosmic microwave background radiation<sup>1</sup> (were this to occur, the gas would absorb heat from the CMB until its temperature rose to 57.3 K).

These runs were performed utilizing 50 processors on the SGI ALTIX machine (Cobalt) at the National Center for Supercomputing Applications (NCSA) at UIUC.

---

<sup>1</sup> $T_{CMB} = 2.73(1+z)K$

# Chapter 3

## Results and Conclusions

### 3.1 The R-Type Front

In Fig. 3.1 we present ionized fraction, density, temperature, pressure, H<sub>2</sub> fraction, and gas velocity profiles along the  $z$  axis through the center of the halo. The I-front enters the computational box from the lower  $z$  face as seen in the plateaus in ionization and temperature to the left of the origin at 200 kyr. Since the temperature in the halo is uniform, pressures rise and fall with density. The front is R-type as shown in the 200 kyr velocity curve in Fig. 3.1 and panel (a) of Fig. 3.2. An R-type front moves supersonically with respect to the gas, propagating through the gas faster than the gas is able to react to it. Thus the halo is still nearly in hydrostatic equilibrium as the front begins to ionize it as evidenced by the relatively undisturbed velocity profile. The normally abrupt ionization profile is broadened by the high energy photons of the star. The spectrum of the star together with the cooling curves of primordial gas set the post front gas temperature to 20,000 K.

By 200 kyr LW photons have broken ahead of the front and dissociated the halo, because the entire H<sub>2</sub> fraction profile is below the setup value of  $2 \times 10^{-6}$  (see also

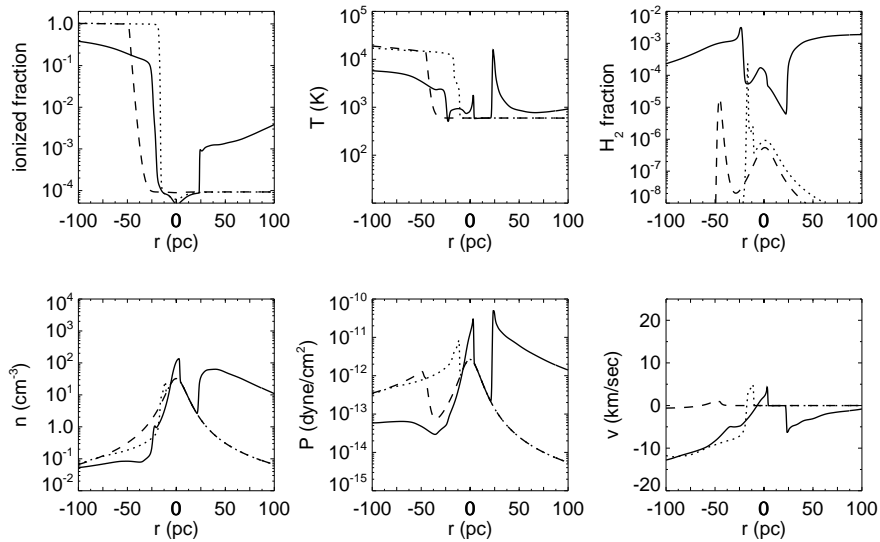


**Figure 3.1** Ionized fraction, density, temperature, pressure,  $\text{H}_2$  fraction and velocity profiles in the TIS halo. Dashed line: 200 kyr, dotted line: 2.4 Myr, solid line: 4.5 Myr.

panel (a) of Fig. 3.3). However, a layer of  $\text{H}_2$  builds in the outer regions of the front, where it is manufactured in the partial ionization there. Free electron fractions of up to 10% and temperatures of 2000–3000 K catalyze its formation on time scales shorter than the dynamical time of the front [22]. This molecular-hydrogen layer later shields  $\text{H}_2$  in the core from the oncoming LW photons.

## 3.2 The D-Type Front

As the I-front climbs the density gradient of the halo it also recedes from the central star. Both effects slow the R-type front to subsonic speeds. The advance of the I-front is preferential above and below the halo where densities are lower; this gives the front the cometary figure in panel (b) of Fig. 3.2. The front remains supersonic above and below the halo but becomes subsonic along the axis. As the front along

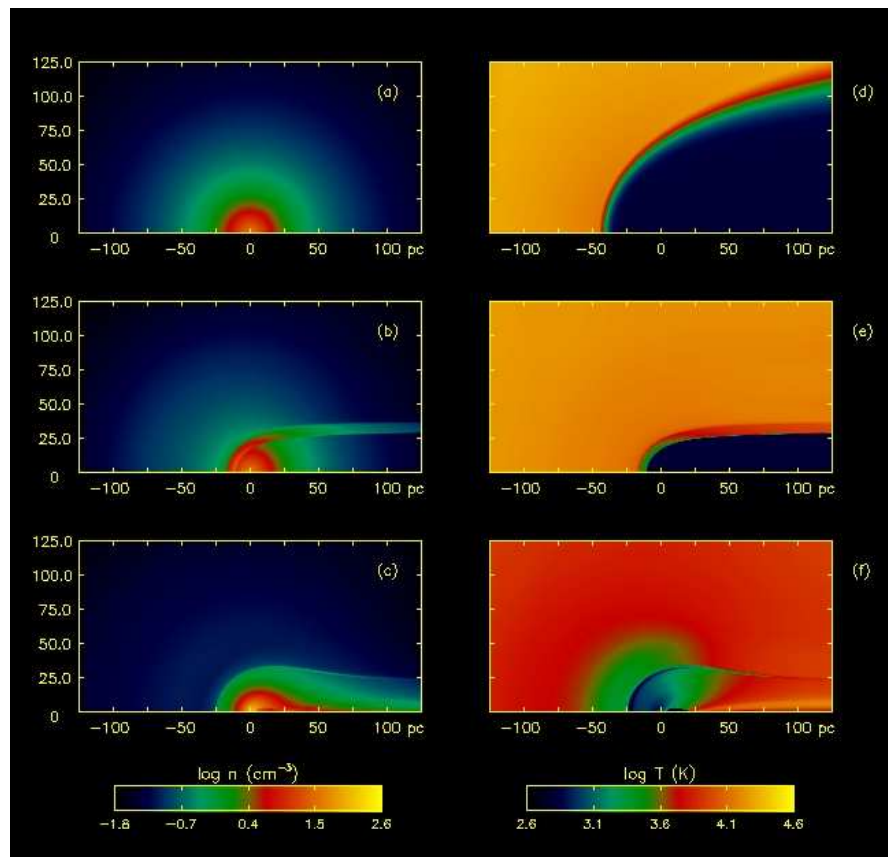


**Figure 3.2** The photoevaporating TIS halo. Panels (a), (b), and (c) are densities at 200 kyr, 2.4 Myr, and 4.0 Myr, respectively. Panels (d), (e), and (f) are temperatures at 200 kyr, 2.4 Myr, and 4.0 Myr, respectively.

the axis slows, a pressure wave grows in the ionized edge that overtakes the front, steepens into a shock, and is driven by the front thereafter, as indicated by the relative positions of the ionization edge and the velocity peak in the 2.4 Myr curves in Fig. 3.1. This is known as a D-type front. As the front drives the shock into the halo the molecular hydrogen fraction between the front and shock rapidly climbs by two orders of magnitude in the  $\text{H}_2$  fraction peak at -24 pc of the 2.4 Myr  $\text{H}_2$  profile. This occurs because the hard UV photons now encounter much larger shock densities that drive fast  $\text{H}_2$  production.

The shock detaches from the front as both advance into the halo. A shell of shocked gas at 2000–3000 K moving at  $\sim 10$  km/s accumulates on the I-front. The shell is subsonic with respect to the 15 km/s sound speed of the ionized gas but subsonic with respect to the 1 km/s sound speed in the pre-shock neutral gas. The rising  $\text{H}_2$  fraction in the front acts as a shutter, protecting the low  $\text{H}_2$  levels in the core from the LW photons from the star. Consequently,  $\text{H}_2$  in the core begins to rise as the minute free electron fraction there once again catalyzes its formation through the  $\text{H}^-$  channel. Comparison of the  $\text{H}_2$  profiles at 200 kyr and 2.4 Myr indicate this  $\text{H}_2$  fraction continues to increase as the front approaches the core. Whether or not the front reaches the core depends on the proximity of the halo to the parent star.

### 3.3 The Relic $\text{H}_2$ Region

At 2.5 Myr, the central star dies, most likely by direct collapse to a black hole [31]. The  $\text{H}_2$  region immediately begins to recombine as seen in the falling ionization fractions in the  $t = 5.0$  Myr profile in Fig. 3.1. Even though the ionized gas cools, the shock continues to advance into the core as shown in panel (f) of Fig. 3.2. Just behind the shock a rarefaction wave forms, visible in the sudden dip in pressure at -10 pc

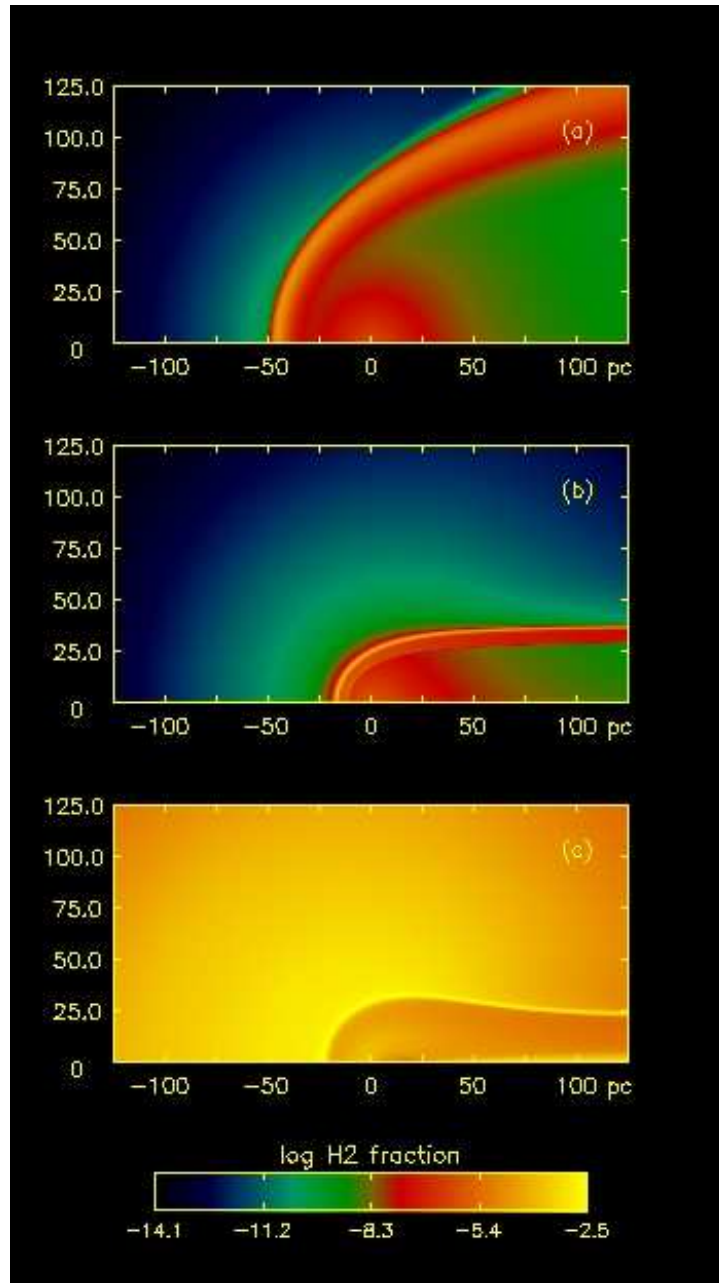


**Figure 3.3**  $H_2$  fractions in the photoionized TIS halo: panels (a), (b), and (c) are 200 kyr, 2.4 Myr, and 4.0 Myr, respectively.

at 5.0 Myr behind the shock. The rarefaction wave drives matter backwards along the negative  $z$  axis. As the shock propagates into the core it slows. The cylindrical implosion reaches the  $z$  axis first far away from the halo but then begins to squeeze it from the right. Rapid  $\text{H}_2$  production ensues in the axial gas because the implosion collisionally ionizes it as shown in panel (c) of Fig 3.3.

As the cylindrical implosion approaches the halo from the right, a shock is driven to the left back to the center. As gas collides on the axis it is compressed and then heated to over 10000 K becoming partially collisionally ionized.  $\text{H}_2$  forms rapidly in this gas, accounting for its sudden appearance at later times to the right of the halo in the 5.0 Myr  $\text{H}_2$  profile. We note this effect is purely due to the radial symmetry of the halo and would not be present in actual three dimensional cosmological halos whose shadows would break the symmetry of the implosion. We point out that this backflow does not interfere with the core of the halo over the time scale of the simulations.

Whether star formation is promoted or quenched in the core depends on the velocity of the shock remnant when it merges with the core. If the remnant, in most cases heavily enriched with  $\text{H}_2$ , arrives at the core with velocities less than 2-3 km/s (the escape velocity from the dark matter halo), most likely the remnant will remain confined to the halo. In such circumstances star formation may be promoted because the final density of the core at 5 Myr is greater than it would have been in the absence of radiation. These higher densities cool, and therefore collapse, more rapidly. If the star is too close, gas may be entirely driven from the core, preventing star formation that would otherwise have occurred. If the star is too far away, the front may not perturb the core at all, having no effect on star formation therein. We note that shielding of the core by the  $\text{H}_2$  in the front does not constitute feedback since it merely allows  $\text{H}_2$  that would have been present in the absence of radiation to re-form. The core of this TIS halo is rattled strongly by the shock but not destroyed.

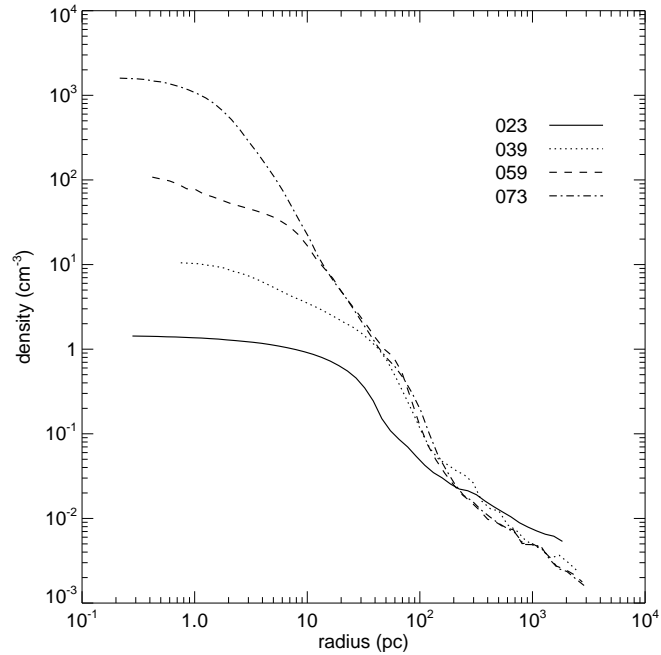


**Figure 3.4** The four halo density profiles used in this study. The redshifts of the 023, 039, 059, and 073 profiles are 23.9, 17.7, 15.6, and 15.0, respectively.

Star formation will probably proceed but be somewhat delayed.

### 3.4 4 Photoevaporation Outcomes

We now consider the four halo profiles derived from the AMR code Enzo. The density and radial velocity profiles for each of the four halos are shown in Figs. 3.4 and 3.5. Whalen *et al* found that the photoevaporated halos have four final fates: (1) complete disruption by an R-type or D-type front; (2) an undisturbed core; (3) density enhancement of the core with clearly accelerated star formation, and (4), denser cores partially exposed to the IGM and eroded over time by ionized backflows [32]. We discuss these four cases below. Their evolution partly parallels that of the TIS halo so the discussion above can serve as a template for these models.

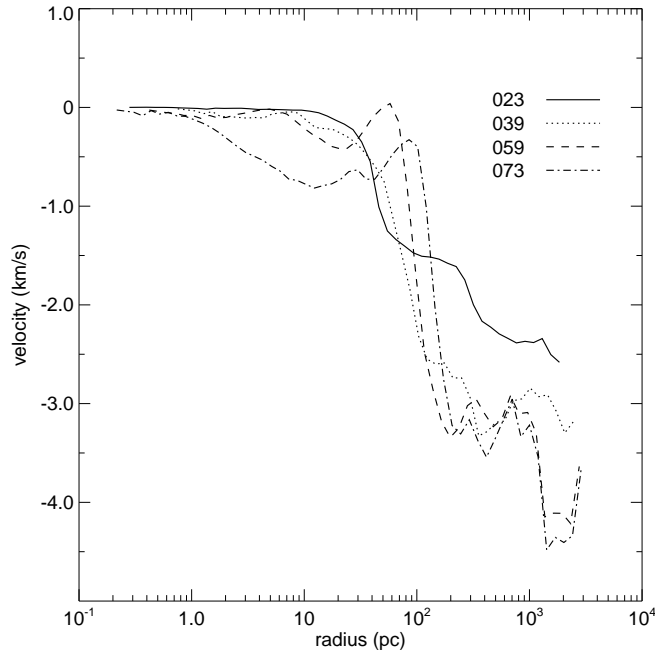


**Figure 3.5** Velocity profiles for the halos used in this study. Within the virial radius ( 100 pc) infall rates are well below the sound speed in the gas.

### 3.4.1 Undisturbed Core

In Fig. 3.6 we present flow profiles along the  $z$ -axis in the 073\_500pc run. This halo has an  $n_c = 1596 \text{ cm}^{-3}$  with the illuminating star at a distance of 500 pc. At 200 kyr the front is still R-type as seen in the 200 kyr density profile. The front becomes D-type at -60 pc. The face of the halo exposed to the star is partly dissociated by its LW photons, but the inner 10 pc is shielded by the high core densities. Molecular-hydrogen fractions at the center of the halo rise from  $2 \times 10^{-6}$  to  $1 \times 10^{-4}$  by catalysis through the H- channel. At the same time, molecular hydrogen rises in the R-type front. The I-front assumes the cometary appearance common to all our runs shown in panel (c) of Fig. 3.7.

Because the halo is very dense, the shadow is compressed toward the  $z$  axis much more slowly than the other halos. The cylindrical shock does not reach the axis by 5

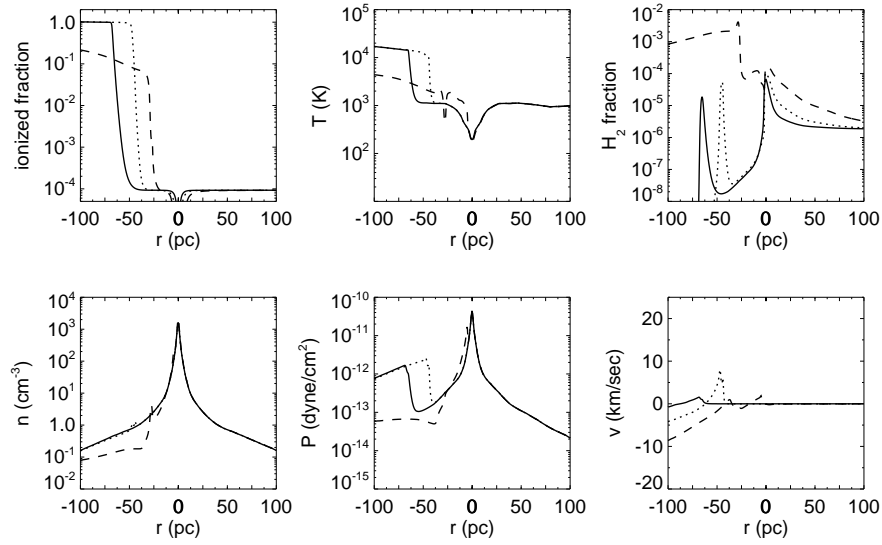


**Figure 3.6** Ionized fraction, density, temperature, pressure,  $H_2$  fraction and velocity profiles for the 073\_500pc model. Solid line: 200 kyr (the R-type front), dotted line: 800 kyr (the D-type front), dashed line: 5.0 Myr (the relic H II region).

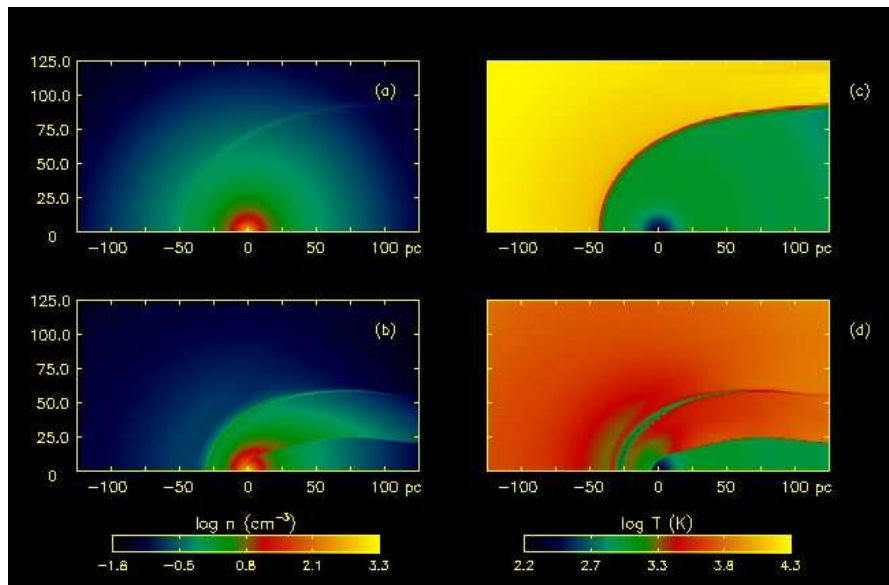


**Figure 3.7** Halo evaporation: model 073\_500pc. Panels (a), (b), and (c) are densities at 800 kyr, 3.09 Myr, and 5.0 Myr, respectively. Panels (c), (d), and (e) are temperatures at 800 kyr, 3.13 Myr, and 5.0 Myr, respectively.

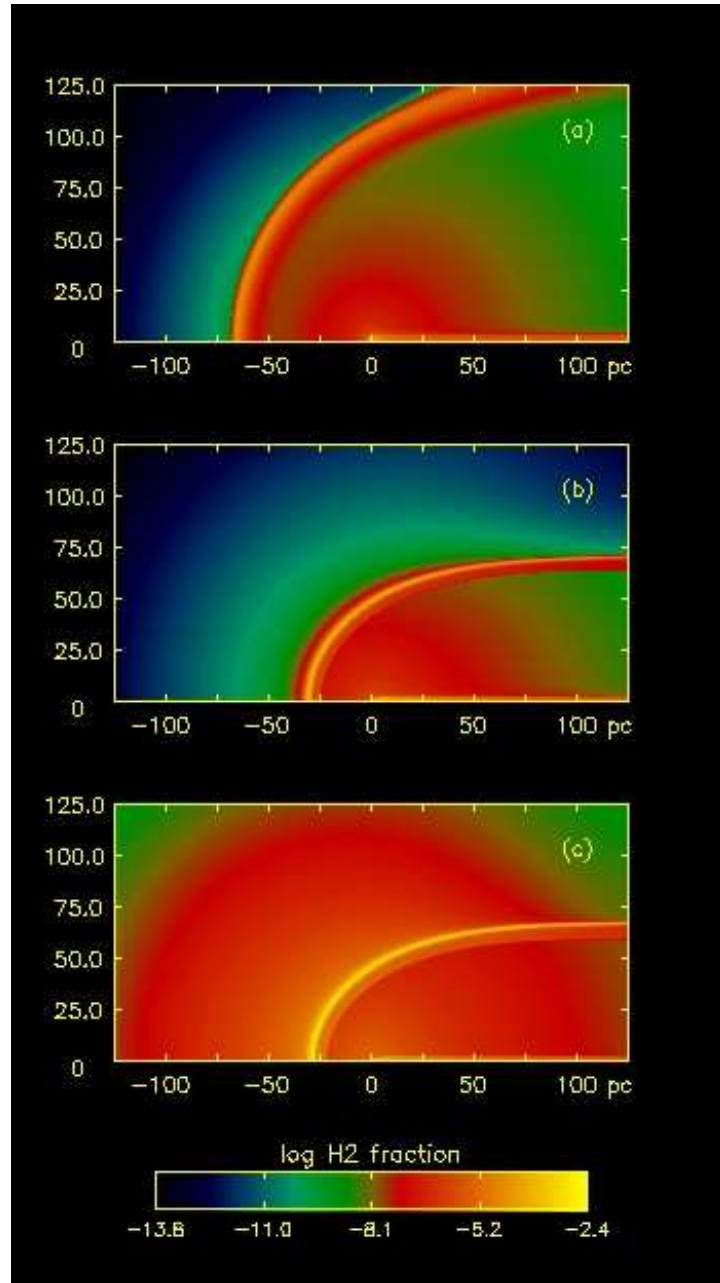
Myr, as shown in panels (b) and (d) of Fig. 3.7. At 2.5 Myr the I-front is 25 pc from the core. Perturbations form at 800 kyr in panel (c) of Fig. 3.7. These fluctuations may be an early stage of an instability that arises in D-type fronts in which UV photons are oblique to the shock.

When recombination occurs at 2.5 Myr,  $H_2$  production occurs rapidly in the shock and quickly spreads throughout the halo as shown in panels (b) and (c) of Fig. 3.8. One interesting feature of the 073 halo is the growth of the Rayleigh-Taylor instabilities at the base of the rarefaction wave in panels (b) and (d) of Fig. 3.7. The shock will ripple through the halo with only minor density fluctuations so star formation is not interrupted there.

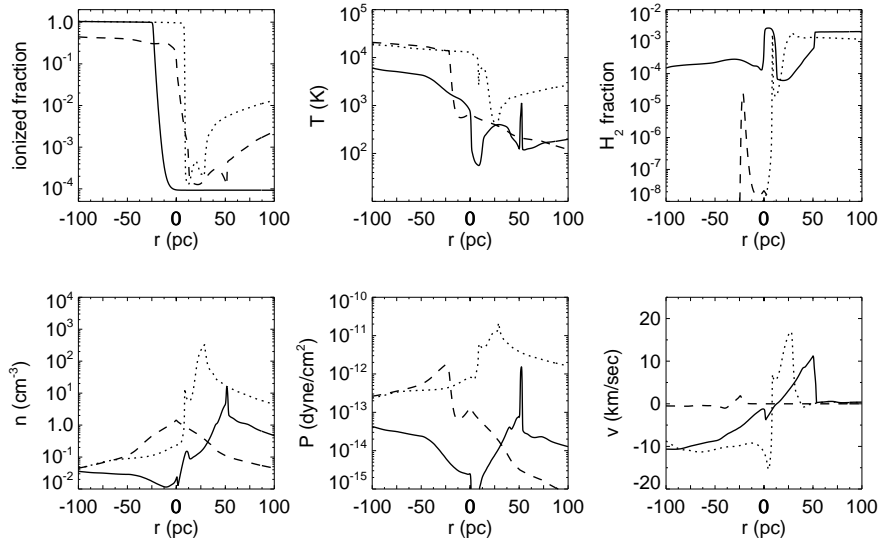
### 3.4.2 Complete Core Disruption

Fig. 3.9 show hydrodynamical profiles for the 023 halo at a distance of 500 pc from the star with  $n_c = 1.43 \text{ cm}^{-3}$ . The  $H_2$  is almost completely dissociated at 225 kyr; only 1% survives, a fraction of  $2 \times 10^{-8}$ . The front becomes D-type  $\sim -20$  pc from the core. The low densities in this halo cannot produce enough  $H_2$  in the shock to adequately shield the core. A very narrow shadow is formed which is crushed almost completely to the  $z$  axis by the death of the Pop III star at 2.5 Myr, as illustrated in Fig. 3.10. This heats the gas to over 15,000 K, causing rapid  $H_2$  production along the axis by collisional ionization as shown in the 2.5 Myr ionization,  $H_2$ , and temperature profiles in Fig 3.9. Molecular hydrogen fractions in the center of the cloud climb to  $2 \times 10^{-3}$  by 2.5 Myr.

Before the star dies, the front pushes the bulk of the gas from the halo 25 pc from the core as seen in the 2.5 Myr density profile in Fig. 3.9, focusing the rest into a small dense fragment that persists on the  $z$ -axis to 5 Myr. The shock displaces this fragment from the core, imparting velocities of 10 km/sec to it in the 5.0 Myr



**Figure 3.8** 073.500pc model: H<sub>2</sub> fractions. Panels (a), (b) and (c) are at 210 kyr, 2.3 Myr, and 2.59 Myr, respectively.



**Figure 3.9** Ionized fraction, density, temperature, pressure,  $H_2$  fraction and velocity profiles for the 023\_500pc model. Dashed line: 225 kyr (the R-type front), dotted line: 2.5 Myr (the D-type front), solid line: 5.0 Myr (the relic H II region).

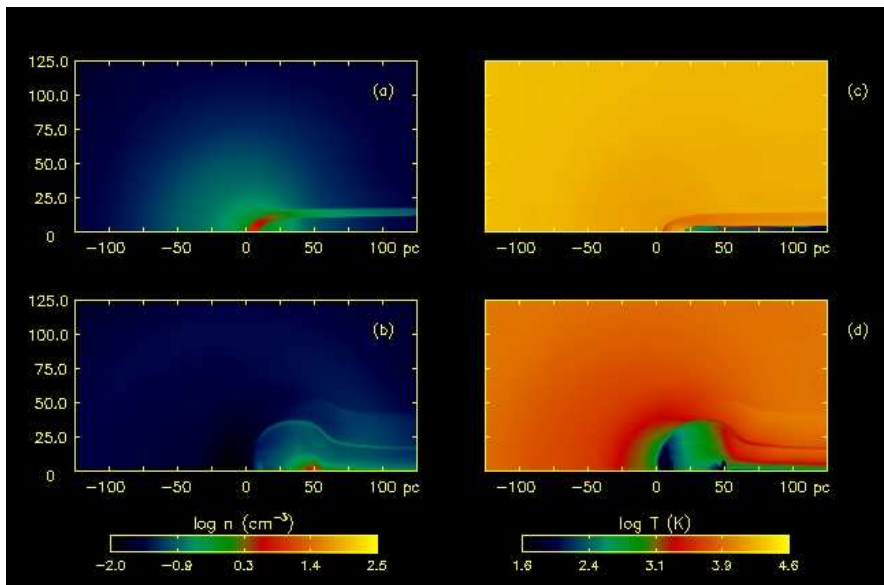


**Figure 3.10** Halo evaporation: model 023\_500pc. Panels (a) and (b) are densities at 1.69 Myr and 5.0 Myr, respectively. Panels (c) and (d) are temperatures at 2.02 Myr and 5.0 Myr, respectively.

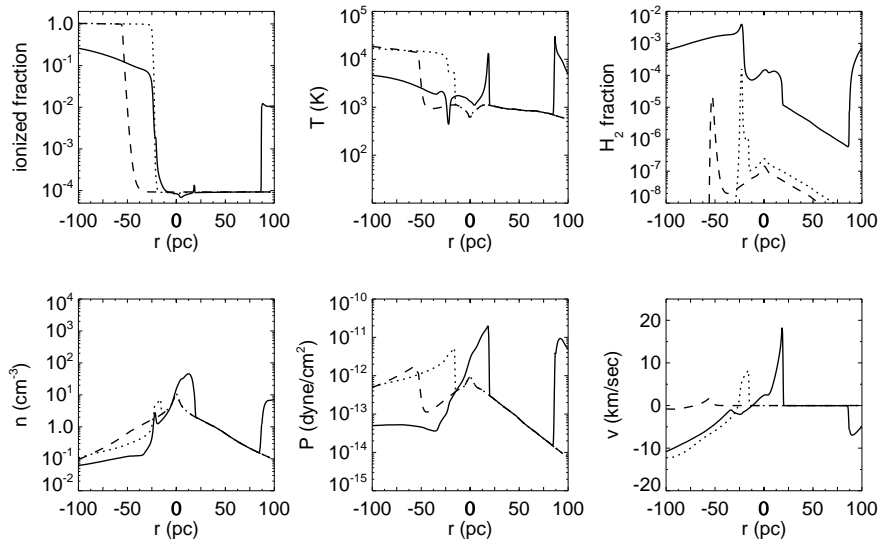


**Figure 3.11** Ionized fraction, density, temperature, pressure,  $H_2$  fraction and velocity profiles for the 039\_500pc model. Dashed line: 225 kyr (the R-type front), dotted line: 2.4 Myr (the D-type front), solid line: 5.0 Myr (the relic H II region).

velocity profile. This clump cannot cool or collapse into a star because it has a mass of  $20 M_{\odot}$ , well below the Jeans mass of  $7.4 \times 10^4 M_{\odot}$  required for a fragment at this temperature and density to fracture and collapse.

### 3.4.3 Accelerated Collapse

In Fig. 3.11 we show profiles for the 039 halo with  $n_c = 10.5 \text{ cm}^{-3}$ . The illuminating star, located 500 pc away, quickly photodissociates the cloud leaving only 5% of the original  $H_2$  in the core at 225 kyr. The front transforms to D-type 40 pc from the center and approaches to within 15 pc of the core at 2.5 Myr. Molecular hydrogen is produced in the shock, which shields the core from LW photons. Comparison of the 225 kyr and 2.5 profiles reveals the  $H_2$  production in the shock and core.

After the death of the star, a jet forms in the warm recombining gas at 20 pc to

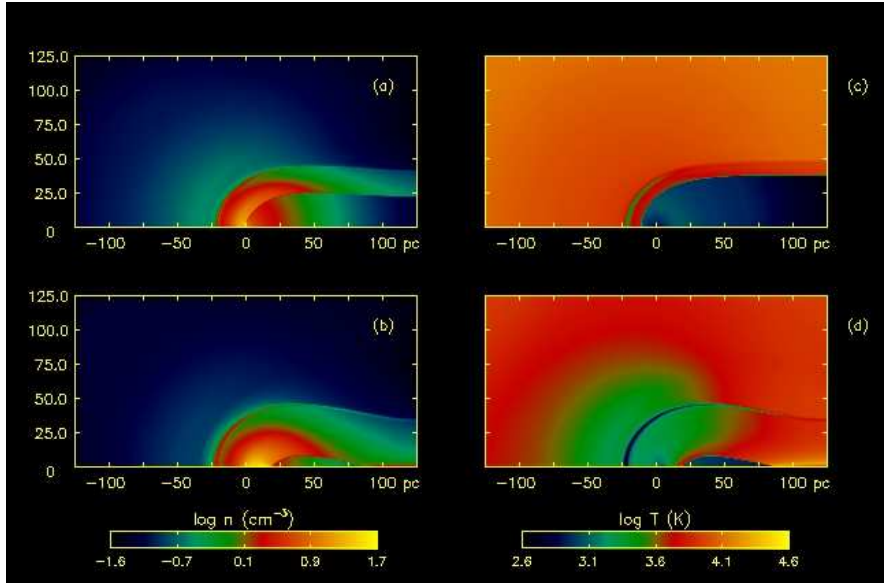


**Figure 3.12** Halo evaporation: model 039\_500pc. Panels (a) and (b) are densities at 3.65 Myr and 5.0 Myr, respectively. Panels (c) and (d) are temperatures at 2.75 Myr and 5.0 Myr, respectively.

the right of the core seen in the 5.0 Myr velocity curve. This gas moves at speeds above the escape velocity and hence will be ejected from the halo. The core gas has also been displaced slightly to the right of the center of the halo, as can be seen in the 5.0 Myr density plot. The density in the core increases to three times its initial value. Under these conditions star formation is expected to be accelerated in the core. The density and temperature panels in Fig. 3.12 reveal two additional features. First, a rarefaction wave detaches from the rear of the halo in the recombinational flow, rapidly cooling as it expands. Second, the shadow simultaneously strikes the  $z$ -axis at two positions,  $z = 15$  pc and  $z = 75$  pc.

Figs. 3.13 and 3.14 show flow profiles for the 059 halo 150 pc from the star. The core is initially dissociated to  $H_2$  fractions of  $\sim 6 \times 10^{-8}$ . The front is R-type at 225 kyr, becoming D-type forming at -20 pc. Molecular hydrogen again forms in the I-front, as seen in the  $H_2$  curves at 50 kyr and 2.5 Myr. The front advances and later

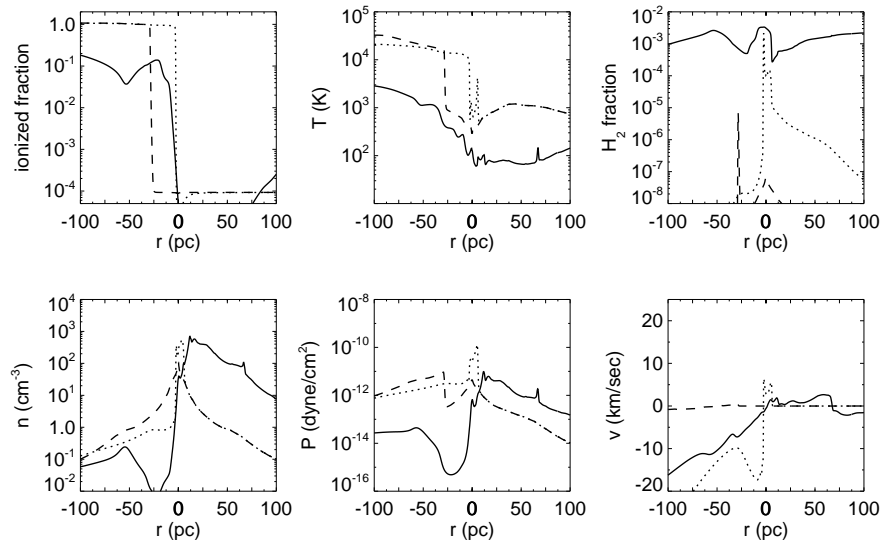


**Figure 3.13** Ionized fraction, density, temperature, pressure,  $\text{H}_2$  fraction and velocity profiles for the 059\_100pc model. Dashed line: 50 kyr (the R-type front), dotted line: 2.5 Myr (the D-type front), solid line: 5.0 Myr (the relic H II region).

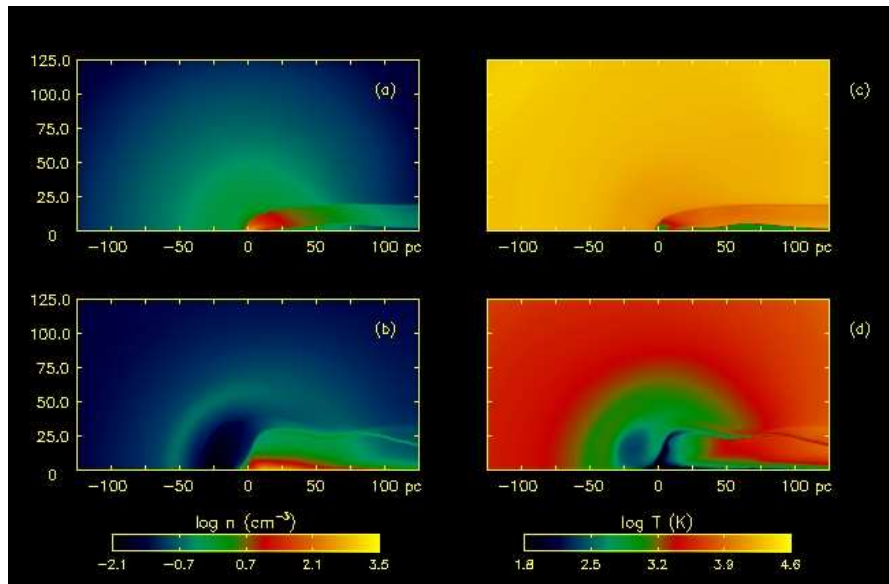


**Figure 3.14** Halo evaporation: model 059\_100pc. Panels (a) and (b) are densities at 2.5 Myr and 5.0 Myr, respectively. Panels (c) and (d) are temperatures at 2.5 Myr and 5.0 Myr, respectively.

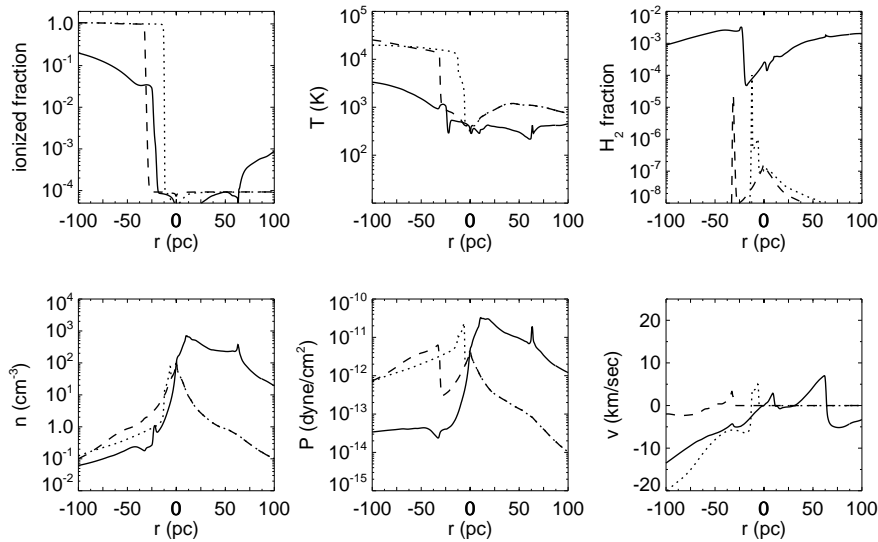


**Figure 3.15** Ionized fraction, density, temperature, pressure,  $H_2$  fraction and velocity profiles for the 059\_250pc model. Dashed line: 225 kyr (the R-type front), dotted line: 2.4 Myr (the D-type front), solid line: 5.0 Myr (the relic H II region).

merges with the core at 2.0 Myr, at which point the core density climbs to  $500 \text{ cm}^{-3}$  and is displaced slightly to the right. At this density the core is able to cool to a temperature of 100 K, optimum conditions for accelerated star formation.

### 3.4.4 Drained Cores

We show in Fig. 3.15 profiles of the 059 halo at a distance of 250 pc from the star. Molecular hydrogen is dissociated to one tenth of its original value at 225 kyr to an equilibrium fraction of  $10^{-7}$ . A D-type shock forms 32 pc from the core. This shock is 7 pc from the core when the star dies at 2.5 Myr and does not shield the core from LW flux. At 2.5 Myr the  $H_2$  profile shows that molecular hydrogen levels in the core are still well below their original value:  $2 \times 10^{-6}$ .

The shock reaches the core at 3.5 Myr, boosting its density from  $108 \text{ cm}^{-3}$  to

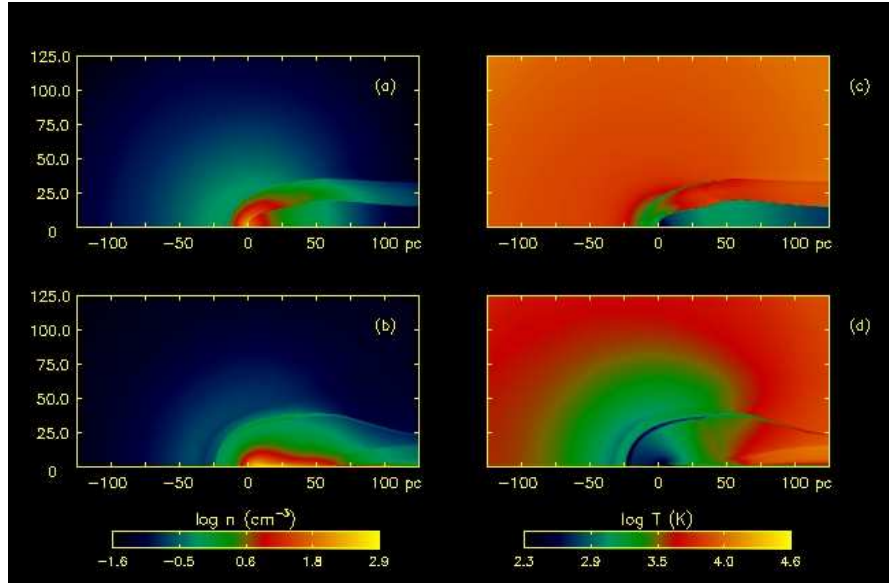


**Figure 3.16** Halo evaporation: model 059\_250pc. Panels (a) and (b) are densities at 3.03 Myr and 5.0 Myr, respectively. Panels (c) and (d) are temperatures at 3.03 Myr and 5.0 Myr, respectively.

$300 \text{ cm}^{-3}$ . In this instance shocked gas both behind and around the core smear the center of the cloud over a few tens of pc along the z-axis. The shock rattles the core, perturbing it to higher densities, but they fall fairly rapidly toward the end of the simulation. The ablation of the halo by the I-front from behind creates strong density gradients to the left of  $z = 0$  that drain gas from the core. Thus, we cannot state with certainty whether a star forms in the center of the cloud remnant. We reserve its future study for high resolution AMR probes currently under development.

## 3.5 Conclusion

Early Population III stars had a variety of effects on star formation in neighboring halos. More evolved halos, with densities greater than  $1600 \text{ cm}^{-3}$ , have cores that are almost completely undisturbed by an oncoming ionization front, with negligible effect

on star formation. Very diffuse halos, especially those close to the illuminating star, are completely destroyed by photoionization and no star forms. Halos of intermediate density are perturbed to varying degrees by the front. In some, shocks form that combine with the core, amplifying its density and  $\text{H}_2$  production through the  $\text{H}^-$  channel and promoting star formation. In others, the core is squeezed out along the z-axis by the shock remnant and the ionized gas surrounding the shadow of the halo, with indeterminate effects on its collapse into a star. The evolution of these halos must be followed at much higher resolution for longer times, perhaps 10–20 Myr, in order to discover their final fate.

Dissociation of  $\text{H}_2$  appears not to have much effect on the clouds. Cores are well shielded in dense halos and are not dissociated. Halos that are fully dissociated by the star regain their  $\text{H}_2$  via the  $\text{H}^-$  channel immediately after the death of the star. At the central densities of this study,  $\text{H}_2$  cooling has little effect on the halo over 2.5 Myr in the absence of radiation, so its loss over the life of the star has little impact.

One limitation of our work is the assumption of radial symmetry. This geometry results in cylindrical implosions whose shocks can affect the core. Such effects will appear in 3D halos but not to the same degree, since their morphologies should break the symmetry of the implosion.

Future work will need to address the effects of density fluctuations on ionization front instabilities. If the I-front encounters halos with density bumps, instabilities may form that penetrate the halos sooner than in our simulations, altering our final results. The effects of time-dependent stellar luminosity on the evaporation of the halo must also be studied. Furthermore, if the star explodes as a supernova, metals from the ejecta may mix with the halo, possibly fracturing it into new stars much smaller than their progenitor. If the star instead collapses to a black hole it may irradiate neighbor halos with hard x rays that partially ionize them, accelerating  $\text{H}_2$

---

production therein and promoting their collapse.

Halo photoevaporation must be revisited in 3D to assess the true role of shadow implosion in core dynamics, as mentioned earlier. We will import a three-dimensional halo computed with Enzo into ZEUS-MP and photoevaporate it over the lifetime of the star. Then the halo will be ported back into Enzo and further evolved after the death of the star with AMR resolution and dark matter and gas dynamics together with primordial chemistry. These simulations will clarify whether stars form in the ambiguous cases discussed earlier. Our present study will enable us to focus our attention on only the likeliest candidates for star-forming halos.



# Bibliography

- [1] C. L. Bennett *et al.*, “First-Year Wilkinson Microwave Anisotropy Probe (WMAP) Observations: Preliminary Maps and Basic Results,” *The Astrophysical Journal Supplement Series* **148**, 1–27 (2003).
- [2] D. N. Spergel *et al.*, “First-Year Wilkinson Microwave Anisotropy Probe (WMAP) Observations: Determination of Cosmological Parameters,” *The Astrophysical Journal Supplement Series* **148**, 175–194 (2003).
- [3] D. N. Spergel *et al.*, “Three-Year Wilkinson Microwave Anisotropy Probe (WMAP) Observations: Implications for Cosmology,” *The Astrophysical Journal Supplement Series* **170**, 377–408 (2007).
- [4] J. C. Mather *et al.*, “A preliminary measurement of the cosmic microwave background spectrum by the Cosmic Background Explorer (COBE) satellite,” *Astrophysical Journal, Letters* **354**, L37–L40 (1990).
- [5] E. L. Wright *et al.*, “Interpretation of the cosmic microwave background radiation anisotropy detected by the COBE Differential Microwave Radiometer,” *Astrophysical Journal, Letters* **396**, L13–L18 (1992).

- 
- [6] W. H. Kinney, E. W. Kolb, A. Melchiorri, and A. Riotto, “Inflationary physics from the Wilkinson Microwave Anisotropy Probe,” *Physical Review D* **69**, 103516–+ (2004).
- [7] H. V. Peiris *et al.*, “First-Year Wilkinson Microwave Anisotropy Probe (WMAP) Observations: Implications For Inflation,” *The Astrophysical Journal Supplement Series* **148**, 213–231 (2003).
- [8] L. Alabidi and D. H. Lyth, “Inflation models after WMAP year three,” *Journal of Cosmology and Astro-Particle Physics* **8**, 13–+ (2006).
- [9] V. Barger, H.-S. Lee, and D. Marfatia, “WMAP and inflation,” *Physics Letters B* **565**, 33–41 (2003).
- [10] L. M. Krauss, “Implications of the Wilkinson Microwave Anisotropy Probe Age Measurement for Stellar Evolution and Dark Energy,” *Astrophysical Journal, Letters* **596**, L1–L3 (2003).
- [11] J. L. Tonry *et al.*, “Cosmological Results from High- $z$  Supernovae,” *Astrophysical Journal* **594**, 1–24 (2003).
- [12] M. Tegmark *et al.*, “The Three-Dimensional Power Spectrum of Galaxies from the Sloan Digital Sky Survey,” *Astrophysical Journal* **606**, 702–740 (2004).
- [13] W. J. Percival *et al.*, “The 2dF Galaxy Redshift Survey: the power spectrum and the matter content of the Universe,” *Monthly Notices of the RAS* **327**, 1297–1306 (2001).
- [14] M. Colless *et al.*, “The 2dF Galaxy Redshift Survey: spectra and redshifts,” *Monthly Notices of the RAS* **328**, 1039–1063 (2001).

- 
- [15] T. Abel, G. L. Bryan, and M. L. Norman, “The Formation and Fragmentation of Primordial Molecular Clouds,” *Astrophysical Journal* **540**, 39–44 (2000).
- [16] T. Abel, G. L. Bryan, and M. L. Norman, “The Formation of the First Star in the Universe,” *Science* **295**, 93–98 (2002).
- [17] S. P. Oh and Z. Haiman, “Fossil H II regions: self-limiting star formation at high redshift,” *Monthly Notices of the RAS* **346**, 456–472 (2003).
- [18] P. R. Shapiro and H. Kang, “Hydrogen molecules and the radiative cooling of pregalactic shocks,” *Astrophysical Journal* **318**, 32–65 (1987).
- [19] M. Ricotti and J. M. Shull, “Feedback from Galaxy Formation: Escaping Ionizing Radiation from Galaxies at High Redshift,” *Astrophysical Journal* **542**, 548–558 (2000).
- [20] M. E. Machacek, G. L. Bryan, and T. Abel, “Simulations of Pregalactic Structure Formation with Radiative Feedback,” *Astrophysical Journal* **548**, 509–521 (2001).
- [21] M. E. Machacek, G. L. Bryan, and T. Abel, “Effects of a soft X-ray background on structure formation at high redshift,” *Monthly Notices of the RAS* **338**, 273–286 (2003).
- [22] M. Ricotti, N. Y. Gnedin, and J. M. Shull, “The Fate of the First Galaxies. I. Self-consistent Cosmological Simulations with Radiative Transfer,” *Astrophysical Journal* **575**, 33–48 (2002).
- [23] M. Ricotti, N. Y. Gnedin, and J. M. Shull, “The Fate of the First Galaxies. II. Effects of Radiative Feedback,” *Astrophysical Journal* **575**, 49–67 (2002).

- 
- [24] H. Susa and M. Umemura, “Secondary Star Formation in a Population III Object,” *Astrophysical Journal, Letters* **645**, L93–L96 (2006).
- [25] K. Ahn and P. R. Shapiro, “Does radiative feedback by the first stars promote or prevent second generation star formation?,” *Monthly Notices of the RAS* **375**, 881–908 (2007).
- [26] B. W. O’Shea, T. Abel, D. Whalen, and M. L. Norman, “Forming a Primordial Star in a Relic H II Region,” *Astrophysical Journal, Letters* **628**, L5–L8 (2005).
- [27] D. J. Whalen, Ph.D. thesis, University of Illinois at Urbana-Champaign, 2006.
- [28] P. Anninos, Y. Zhang, T. Abel, and M. L. Norman, “Cosmological hydrodynamics with multi-species chemistry and nonequilibrium ionization and cooling,” *New Astronomy* **2**, 209–224 (1997).
- [29] T. Abel, P. Anninos, Y. Zhang, and M. L. Norman, “Modeling primordial gas in numerical cosmology,” *New Astronomy* **2**, 181–207 (1997).
- [30] H. Kirchoff, *Philos. Mag.* **19**, 193 (1860).
- [31] A. Heger and S. E. Woosley, “The Nucleosynthetic Signature of Population III,” *The Astrophysical Journal* **567**, 532–543 (2002).
- [32] D. Whalen, J. Smidt, B. O’Shea, and M. L. Norman, “Photoevaporation Of Satelllite Halos By The First Stars,” *The Astrophysical Journal Submitted* (2007).